communications physics

A Nature Portfolio journal

Article

https://doi.org/10.1038/s42005-025-02263-2

Experimental evidence of non-equilibrium phase separation in supercritical fluids

Check for updates

Juho Lee [1], Yeonguk Kim[1], Jong Dae Jang[2], Changwoo Do [3], Min Young Ha [4] & Gunsu Yun [1,5]

Supercritical fluids (SCFs), widely utilized in many industries, have long been regarded as homogeneous single-phase media. Recent simulation studies identified different phases (more gas-like or liquid-like) in SCFs at equilibrium, expanding the previous notion but still not addressing non-equilibrium properties of SCFs. Here we reveal the existence of long-lived liquid-like clusters in non-equilibrium SCFs by time-resolved small-angle neutron scattering measurements. Since SCFs in industrial applications frequently operate under dynamic, non-equilibrium conditions rather than strict thermodynamic equilibrium, our findings offer crucial information for improving the use of SCFs in industrial settings, like semiconductor cleaning and plant thermal-hydraulic engineering.

Supercritical fluids (SCFs) have long been understood as single-phase systems, distinct from subcritical fluids that exhibit clear liquid and vapor phases. Due to their homogeneous and structureless nature, SCFs are typically regarded as fluids with negligible surface tension and no phase transition. However, recent studies have demonstrated that SCFs can exhibit liquid-like or gas-like properties depending on variations in pressure, temperature, and density[1–11]. These variations, although continuous, are associated with phenomena such as sound dispersion, unexpected fluctuations in thermodynamic response functions, and density correlations. The SCF regime at equilibrium can be divided into several sub-regimes separated by the Widom line and Frenkel line. The Widom line is an extension of the liquid-gas coexistence curve beyond the critical point, representing the locus of maximum thermodynamic response functions such as heat capacity and compressibility[1,2]. The Frenkel line is defined where the time for a particle to move by its size equals the shortest transverse oscillation period[3,4,7]. It distinguishes a rigid liquid, where particle motion exhibits solid-like vibrations, from a nonrigid gaslike fluid, where only uncorrelated ballistic motion dominates. Crossing the Frenkel line on temperature increase (pressure decrease) results in the specific heat reaching $2k_B$, the disappearance of shear rigidity, and the qualitative change of temperature and pressure dependencies of the sound speed, diffusion coefficient, viscosity, and thermal conductivity[3,4,12,13]. Although discussions on the nature of those smooth transitions have greatly expanded the physical understanding of SCFs in equilibrium, the notion of well-defined phase boundaries remains somewhat controversial and continues to be the subject of active discussion[7,14,15]. Moreover, the behavior of SCFs under non-equilibrium conditions remains poorly understood.

Many industrial applications, such as SCF extraction[16,17], rocket engines[18] and high-pressure fuel injection systems, involve highly dynamic non-equilibrium processes, where spatial and temporal variations occur rapidly. In high-pressure fuel injection, for instance, SCFs undergo continuous changes in their thermodynamic and transport properties alongside abrupt transitions like ligament and droplet formation[18]. In the transcritical regime, these phenomena create an ambiguous boundary between single-phase and two-phase behavior, underscoring the necessity for systematic investigations into the non-equilibrium properties of SCFs. Beyond industrial applications, non-equilibrium SCF dynamics are also observed in planetary meteorology. For example, the thick atmosphere of Venus consists of SCFs undergoing complex convective and turbulent flows, where rapid thermodynamic changes influence large-scale atmospheric circulation patterns. Understanding these processes requires further exploration of SCF behavior under extreme conditions.

Recently, the non-equilibrium behavior of single-component SCFs has been explored by measuring submicron-sized liquid-like droplets persisting in an argon SCF background[19]. This study indicates that the extended lifetime of droplets is strongly influenced by the presence of smaller liquid-like particles, known as clusters. These clusters play an essential role in explaining the opacity of high-pressure SCFs and the surprisingly long lifespan of droplets, which can survive up to approximately an hour. Moreover, SCFs with dense, inhomogeneous particles are reported as a promising medium for generating strongly coupled plasmas and extending their lifetimes[20]. However, while the existence of clusters is theorized, direct experimental evidence of nanometer-scale particles in SCFs has not yet been demonstrated.

These clusters, which form through adiabatic expansion and cooling, persist as liquid-like fluid packages before evaporating into the gas-like background. These findings challenge the conventional understanding of SCFs as purely homogeneous systems and suggest that non-

[1]Department of Physics, POSTECH, Pohang, Republic of Korea. [2]Neutron Science Division, Korea Atomic Energy Research Institute, Daejeon, Republic of Korea. [3]Neutron Scattering Division, Oak Ridge National Laboratory, Oak Ridge, TN, USA. [4]Department of Chemical Engineering, Kyung Hee University, Yongin, Republic of Korea. [5]Division of Advanced Nuclear Engineering, POSTECH, Pohang, Republic of Korea. e-mail: gunsu@postech.ac.kr

equilibrium dynamics can drive the emergence of distinct microstructures within SCFs.

The presence of clusters in SCFs may influence mass transport processes in dense planetary atmospheres, such as those of Venus and Jupiter, as well as in engineering applications like power plant cooling systems, pharmaceutical processes, and high-pressure fuel injection. Additionally, these phenomena could play a role in SCF CO_2 cleaning techniques for semiconductor fabrication, where transient clustering might impact process efficiency. In this study, we employed opacity measurements and small-angle neutron scattering experiments to provide direct evidence of long-lived, liquid-like clusters in SCFs. Our findings reveal that these clusters dissolve slowly over extended timescales, offering insights into the non-equilibrium phase behavior of SCFs and advancing the understanding of their dynamic properties.

Results

Experimental apparatus and conditions

The pressure inside of the high-pressure chamber is increased by the compressor, which consists of the rotating motor and two pistons with check valves. When the motor rotates one cycle, the pistons compress the gas and eject through the check valve opening at the 300 bar. These pistons operate about 4.1 Hz and supply 6.8 cm^3 fluid in each cycle. Figure 1a shows the schematic figure of the experimental setup to measure the opacity of SCFs. The high-pressure chamber has five sapphire windows for optical diagnosis, and can hold upto 300 bar pressure without leaking. The opacity is calculated by the ratio between the incident and transmitted laser power (633 nm, He-Ne laser).

The small angle neutron scattering (SANS) experiments were conducted at the 40-m SANS beamline at the HANARO experimental reactor[21]. The neutron wavelength was 6 Å, and the sample-to-detector distance of 1.16 m was chosen to explore nanometer-scale features in the krypton SCF. The q-range spans approximately 0.01 to 0.6 $Å^{-1}$. The specially designed high-pressure cell for the neutron beam experiment can contain SCF pressure of up to 100 bar. Unlike solid and polymer samples commonly used in neutron scattering experiments, SCFs have lower density and smaller scattering cross-sections, making signal detection more challenging. A sample thickness of 5 mm was implemented to increase the scattering volume. Aluminum windows were chosen to minimize neutron absorption and scattering noise while ensuring safety at high pressure. However, they produce non-negligible scattering at low q. This was not a significant issue, as the clusters of interest primarily appear at higher q values, where the aluminum background is less relevant. The windows have a clear aperture of 16 mm diameter and a thickness of 1 mm. The SANS experiment was performed on krypton because it generated the largest number of clusters, as indicated by optical measurements (see Fig. 1). Additionally, while argon has a neutron scattering cross-section of 0.683×10^{-24} cm^2, krypton has a significantly higher cross-section of 7.68×10^{-24} cm^2, making it more favorable for scattering signal detection[22]. To observe the time-dependent evolution of clusters, SANS data was collected every minute. The data has been corrected for detector sensitivity and electrical noise. The 1D scattering intensity was obtained by azimuthally averaging the measured 2D isotropic scattering data. Data points in the low-q and high-q regions, where measurement errors are significant due to detector edge artifacts, were excluded.

Generation of liquid-like particles by temperature drop

The opacity of SCFs was measured to demonstrate how their properties change with pressure. The initial He-Ne laser power, I_0, and the transmitted

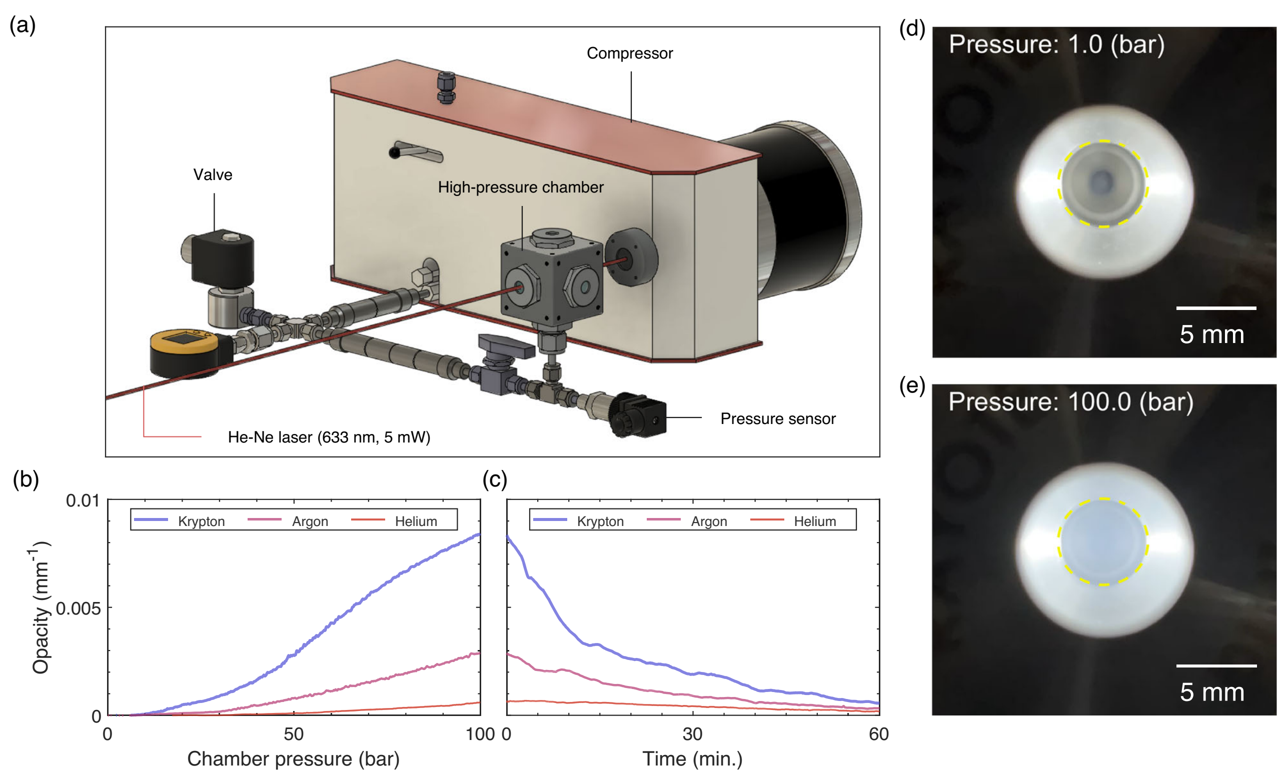

Fig. 1 | Experimental apparatus and opacity measurements. **a** Schematic of the high-pressure chamber system, created using the 3D design software. The He-Ne laser (633 nm, 5 mW) is used to measure the scattered and transmitted signals. Some high-pressure components (hoses and connectors) are modeled using publicly available CAD files from Swagelok. **b** Medium opacity within the high-pressure chamber at time zero. Increased opacity indicates the presence of dense particles that scatter the laser. **c** Time dependence of medium opacity at 100 bar. The turbidity inside the chamber gradually decreases, becoming transparent over time. **d**, **e** Images inside the chamber during the compression process using argon. The pressure corresponds to 1 bar and 100 bar, respectively. The yellow dashed circle indicates the opposite side of the chamber, which is the gas inlet. A scale bar of 5 mm is shown in each panel.

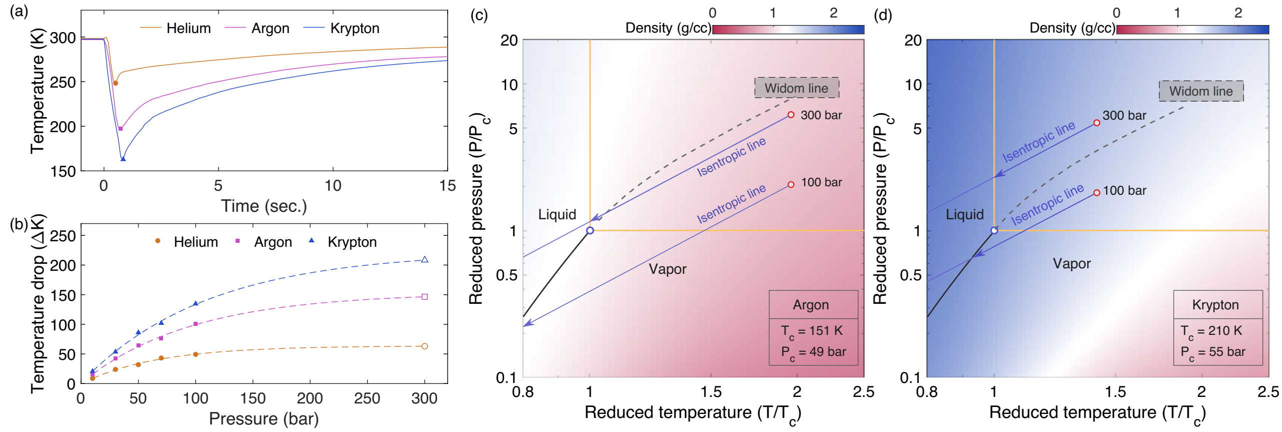

Fig. 2 | Formation of liquid-like particles by a temperature drop of expanding fluids. **a** The experimental measurement for fluid temperature when 100 bar fluid in a high-pressure chamber suddenly expands into a 1 bar environment. The final temperature varies significantly depending on the fluid species. **b** Minimum temperatures for different chamber pressures. A temperature drop of 50 K, 150 K, and 200 K is expected for helium, argon, and krypton, respectively, at the operating pressure of the check valve (300 bar). **c**, **d** Phase diagram of argon and krypton in equilibrium. Since the compressor operates at a working pressure of 300 bar, the fluid expands into the hose with a relatively lower pressure, leading to cooling. The corresponding isentropic lines are represented by solid lines and arrows. The Widom line, indicated by a dashed line, is drawn by connecting the loci of maxima in the isobaric heat capacity. The thermophysical data are obtained from the NIST Chemistry WebBook[29].

power, I, were measured to calculate the opacity using the equation:

$$I = I_0 \exp(-\kappa d), \tag{1}$$

where κ represents the opacity, and d is the distance the laser travels through the SCF sample medium. Figure 1b shows that the opacity inside the chamber increases as pressure increases. Figure 1d, e are the photos looking inside the high-pressure chamber, captured during the compression process (Supplementary Movie 1). It shows a significant change of opacity depending on pressure. The 100 bar SCF is too opaque to observe the other side of the chamber. The enhanced scattering from high-pressure SCF arises from the generation of dense particles, rather than from the increase in particle density, which is approximately proportional to the pressure. Figure 1c underpins the generation of liquid-like particles during the compression process. When the pressure inside the chamber reaches 100 bar, fogginess is observed, which gradually diminishes over time. Transparency is almost restored after one hour. Thus, the increase in opacity is a temporary phenomenon associated with non-equilibrium phase coexistence, analogous to the evaporation process in the subcritical regime.

The contribution of scattering from the generated clusters to the observed opacity can be estimated using the Rayleigh scattering cross-section. The scattering cross-section of an individual cluster is given by:

$$\sigma = \frac{2\pi^5}{3}\frac{(2r)^6}{\lambda^4}\left(\frac{n^2-1}{n^2+2}\right)^2, \tag{2}$$

where r is the radius of particle, λ is the wavelength of the incident light, and n is the refractive index ratio between the scattering particle and the surrounding medium[23,24]. The opacity due to scattering is given by $\kappa_s = n_s \times \sigma$, where n_s is the number density of the particle species. Assuming that the refractive index of liquid krypton at 150 K is $n \sim 1.3$[25], we can estimate the possible size and density range if their scattering contribution dominates the measured opacity.

Meanwhile, direct imaging of the clusters is not feasible because they are much smaller than the diffraction limit of the 633 nm He-Ne laser. Therefore, to obtain direct evidence of these small particles, we conducted SANS experiments, which will be discussed in the following sections.

The opacity level varies among species. Krypton exhibits a significant increase in opacity, whereas helium remains unchanged from its initial level at 1 bar. This difference arises from variations in their thermophysical properties. The formation of dense liquid-like particles, or clusters, is attributed to localized cooling caused by adiabatic expansion at the compressor outlet. Therefore, the location of the final temperature and pressure point in phase diagrams after the expansion process is essential. Using helium, argon, and krypton gases, we measured the temperature drop for each fluid to quantify the adiabatic expansion process from high pressure to atmospheric pressure. A thermocouple is positioned 10 mm from the outlet of the high-pressure chamber. As shown in Fig. 2a, the fluid temperature drops sharply when the valve opens. Despite undergoing the same pressure change, the magnitude of the temperature drop is different depending on the fluid species. Figure 2b shows the temperature change as a function of chamber pressure. The check valve inside the compressor opens at 300 bar, which implies that the temperature of krypton is expected to drop by more than 200 K. Such a significant temperature drop would facilitate formation of the liquid-density particles during the expansion process. This is further examined through the reduced phase diagrams of argon and krypton in their equilibrium states, shown in Fig. 2c, d. Along the isentropic lines depicted in the phase diagrams, the temperature decreases, and upon reaching the liquid phase, a phase transition to the liquid state occurs. Although the measured temperature drop does not perfectly correspond to that predicted by ideal adiabatic expansion, the minimum temperature experienced by the fluid in the compressor clearly falls within the liquid-phase region of the phase diagram. The transition into the liquid phase occurs more readily in krypton than in argon, which is consistent with the higher opacity observed for krypton in Fig. 1b. In contrast, helium exhibits a much smaller temperature drop, and its liquid-gas coexistence line is too far from room temperature, preventing it from reaching the liquid phase.

As demonstrated, the expansion process in the compressor induces a significant temperature drop, leading to the formation of liquid-like clusters. In the case of krypton, the temperature can decrease to approximately 150 K when the pressure drops from 100 bar to 1 bar. Nevertheless, the temperature of the stainless steel high-pressure hose and chamber remains at room temperature. The pistons in the compressor, operating at 4.1 Hz, introduce krypton fluid at a rate of approximately 1.1×10^{-3} mol · s^{-1}. The power required to heat the fluid from 150 K to 300 K is estimated as

$$P_{\text{heat}} = C_p \cdot N \cdot \Delta T \approx 4.2\,\text{W}, \tag{3}$$

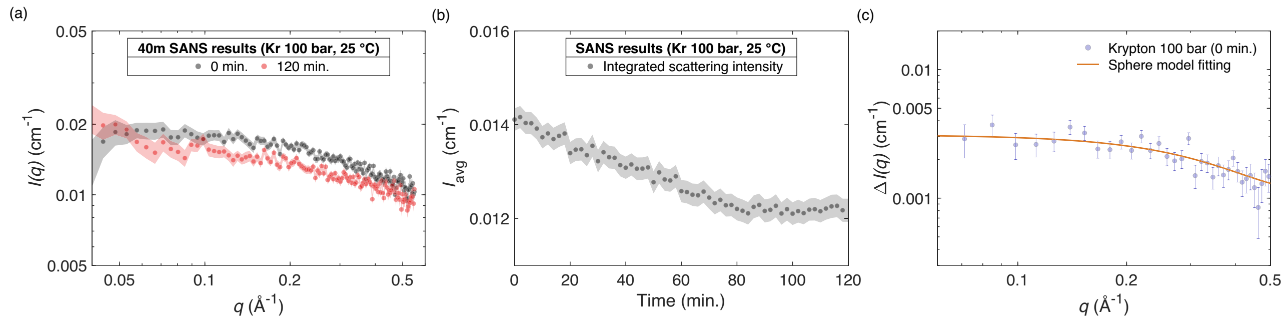

Fig. 3 | Neutron scattering signal over time. a After compression, the SANS signal is measured over time. The horizontal axis shows the scattering vector q, and the vertical axis shows the scattering intensity $I(q)$. The scattering intensity measured at 2 h after the compression shows distinct decrease in scattering intensity. **b** Time evolution of the scattering signal integrated over the entire q-range of 0.02–0.5 $Å^{-1}$. The vertical axis represents the averaged scattering intensity, I_{avg}. The scattering intensity gradually decreases over time and saturates around 80 min. **c** Spherical model fitting results. The fitting analysis uses the difference between the scattering signals at 0 and 120 min so the vertical axis represents the difference of scattering intensity ΔI. The orange line represents the fitting result, corresponding to scattering from liquid-like particles with a diameter of 1.3 nm. The error is represented as shaded regions for (**a**, **b**), and as error bars for (**c**). The errors in all panels reflect both the statistics of scattered neutrons and the standard deviation arising from the circular averaging process within each q-bin.

where the average heat capacitance $C_p \sim 25.5\ \mathrm{J \cdot K^{-1} \cdot mol^{-1}}$ within the given temperature range under 10 bar. In contrast, the heat transfer rate of the entire system is significantly higher. Even with a conservative assumption of $\delta T \sim 10$ K, the heat transfer rate is estimated as

$$\frac{dQ}{dt} \sim k\frac{2\pi rL}{d}\delta T \sim 160\ \mathrm{W}\,, \tag{4}$$

where the thermal conductivity of a stainless steel $k \sim 16\ \mathrm{W \cdot m^{-1} \cdot K^{-1}}$, demonstrating that the system's heat transfer rate far exceeds the power required to restore the injected fluid to room temperature. As a result, although the incoming fluids have a low enough temperature for liquid-phase formation, the overall system remains at room temperature.

Observing the temperature decrease caused by repeated adiabatic expansion in the compressor and the changes in opacity inside the high-pressure chamber indicate the presence of a large number of liquid-density particles and their stable persistence within high-pressure SCFs. However, aside from indirect estimations, no direct experimental observation of these clusters has been reported. Here, we utilize a neutron beam to investigate the existence and physical properties of these nanometer-sized clusters.

Small-angle neutron scattering results

SANS is a powerful tool for analyzing the properties of nanometer-scale particles and structures[26]. Figure 3 shows the neutron scattering results obtained using krypton. Comparing the neutron scattering signals measured immediately after pressurization and 120 min later reveals a substantial difference in signal intensity within the given q-range. Figure 3b shows the time evolution of the neutron scattering signal, integrated over the entire q-range of 0.02–0.5 $Å^{-1}$. Despite maintaining the same pressure and temperature conditions, the scattering intensity gradually decreases over time and levels off after approximately 80 min. The scattering intensity is proportional to the scattering contrast ($\Delta\rho$) and the volume fraction (v) of the particles:

$$I(q) \propto \Delta\rho^2 v. \tag{5}$$

The scattering contrast is given by

$$\Delta\rho = \rho_{\mathrm{l}} - \rho_{\mathrm{g}}, \tag{6}$$

where ρ_{l} and ρ_{g} are the scattering length densities of the liquid-like clusters and the gas-like SCF, respectively. Since the scattering length densities of the clusters and the background medium can be assumed to remain constant, the integrated scattering intensity reflects the volume fraction of the particles. Thus, the gradual decrease in intensity indicates that the clusters responsible for the scattering signal gradually dissolve over an hour.

A measurable slope of the scattering signal is observed even after 120 min, indicated by the red points in Fig. 3a. This signal arises from density fluctuations inherent to the high-pressure krypton SCF. For reference, the correlation length in supercritical CO_2 and xenon typically ranges from a few angstroms to tens of angstroms, depending on the condition[27]. To better understand the shape and size of the clusters, we subtracted the scattering contribution from SCF density fluctuations. As shown in Fig. 3c, the scattering signal is well-fitted by the sphere particle model. The solid line corresponds to a fitting result of a liquid-like krypton particle with an estimated diameter of 1.3 nm, suggesting that it consists of around 30 krypton atoms clustered together.

Discussion

Our results provide direct experimental evidence of non-equilibrium phase separation in SCFs. The gradual decrease in scattering intensity over time indicates that liquid-like clusters progressively disappear. It raises a question: how do clusters evaporate into the background SCF? Do they disappear while maintaining their size distribution, or does their size decrease while their number remains constant? Since the fitting of the measured scattering signal represents the average cluster size distribution, analyzing its evolution over time can provide insight into this process.

Figure 4 shows the scattering signal from clusters over time with the corresponding fitting results. Similar to Fig. 3c, this plot shows scattering from the krypton clusters after SCF background subtraction. Initially, the signal is strong but gradually weakens, with increasing error bars. The decrease in volume fraction due to cluster dissipation leads to a reduction in scattering intensity. After approximately 30 min, the overall shape of the graph changes, suggesting an increase in the polydispersity of the cluster size distribution. In liquid evaporation, particle exchange at the surface plays a key role, and smaller particles tend to evaporate more quickly due to their higher surface-to-volume ratio. Consequently, as evaporation progresses, larger particles persist longer while smaller ones disappear, leading to a gradual broadening of the size distribution. As a result, while the early-time signal is well described by a uniform sphere model, the later-time requires consideration of size distribution broadening. This implies that as clusters evaporate, their average size decreases while the overall distribution widens. Figure 4b illustrates the estimated evolution of the cluster size distribution over time. The initial distribution at 0 minutes is assumed to be a Gaussian function with a narrow standard deviation. Its mean value is determined based on the fitting results, while the changes in standard deviation and peak height are determined using the total scattering intensity data from Fig. 3b. The total scattering intensity at 0, 30, and 60 min follows a ratio of 1:0.52:0.25, which corresponds to the volume fraction of scattering particles.

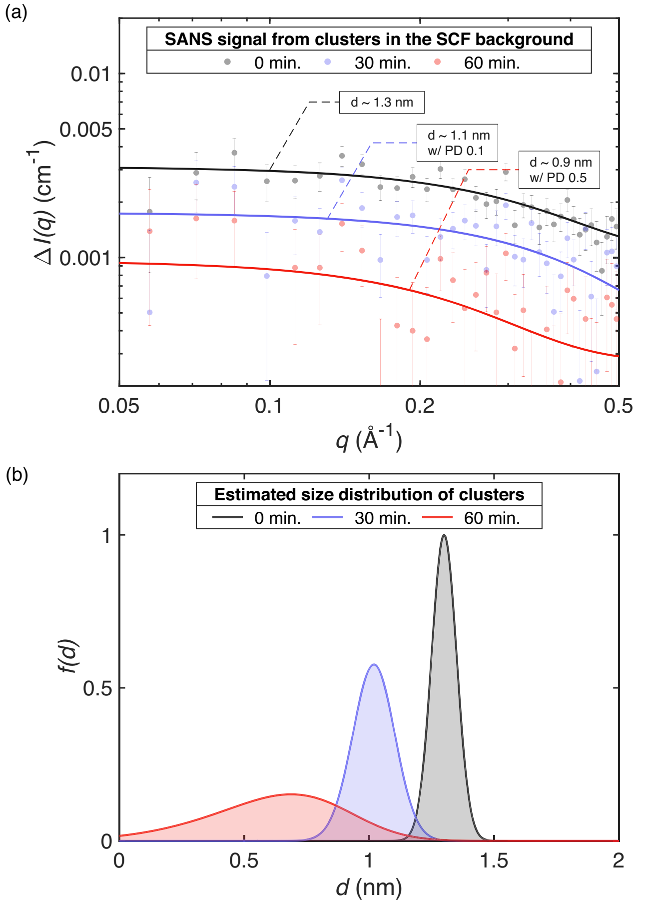

Fig. 4 | Time evolution of the scattering signal and cluster size distribution. **a** Scattering signal at different time points (0 min, 30 min, and 60 min). The horizontal axis shows the scattering vector q, and the vertical axis shows the difference in scattering intensity ΔI(q). The data measured at 120 min, where the signal no longer decreases, is used as a baseline, and the plotted curves represent the difference from this background. The scattering intensity decreases over time, with increasing error bars, indicating growing uncertainty in the late-time measurements. The fitted curves suggest a reduction in average cluster size over time, accompanied by increasing polydispersity (PD). For the 60-min data (red curve), the fit includes a PD value of 0.5, reflecting an increased spread in cluster size distribution. The error bars represent the combined uncertainty from neutron counting statistics and the standard deviation arising from the circular averaging process within each q-bin. **b** Schematic representation of the expected evolution of the cluster size distribution, where the horizontal axis d and the vertical axis represent cluster diameter and distribution function, respectively. Based on the decreasing cluster size, the distributions are estimated to shift toward smaller sizes over time while increasing polydispersity.

Since volume fraction depends on the number density of particles and their volumes, the time-dependent size distribution is adjusted so that the product of the integrated distribution (particle number) and the total volume of the particles satisfies this ratio. This ensures a physically consistent representation of how the size distribution broadens and shifts as clusters dissipate over time. However, it remains uncertain whether considering polydispersity is the most appropriate approach, as consideration of polydispersity poses a challenge for signal interpretation[26,28]. This challenge becomes severe in a weak signal, such as the scattering signal at 60 minutes, making precise analysis difficult. Nevertheless, understanding how clusters evolve is essential for capturing the dynamics of their dissipation. In this regard, we hope our study serves as a milestone for further investigations into non-equilibrium phase separation.

The previous SANS measurements are conducted while maintaining the temperature of the background gas-like krypton SCF at room temperature (25 °C). If the decaying clusters are analogous to the evaporation process in the subcritical region, this behavior is expected to depend on the temperature of the surrounding medium. To investigate this, we lowered the sample temperature to 10 °C by adjusting the stage temperature of the high-pressure chamber. As shown in Fig. 5, the results reveal an intriguing contrast to the previous results at room temperature. When the background SCF is at a lower temperature, the neutron scattering signal remains stable rather than decreasing, indicating that the krypton clusters persist much longer and maintain their opaque state. The less pronounced change in the SANS signal suggests that clusters are more stably maintained at lower temperatures. One possible reason is that the system is thermodynamically closer to the crossover regime associated with the Widom line, which separates gas-like and liquid-like behaviors in SCFs. 10 °C lies closer to this line than 25 °C under the same pressure. Moving toward the Widom line may enhance the thermodynamic stability of liquid-like clusters and facilitate their survival. Additionally, reduced kinetic energy at lower temperatures may lead to less frequent or less energetic collisions from surrounding particles, potentially contributing to longer cluster lifetime. Although the precise mechanism behind the temperature dependence of cluster dynamics is not yet fully understood, this observation highlights the need for molecular-level understanding of cluster dynamics and mass transport. Future investigations, such as molecular dynamics simulations, may help clarify how cluster stability evolves under near-equilibrium or non-equilibrium conditions.

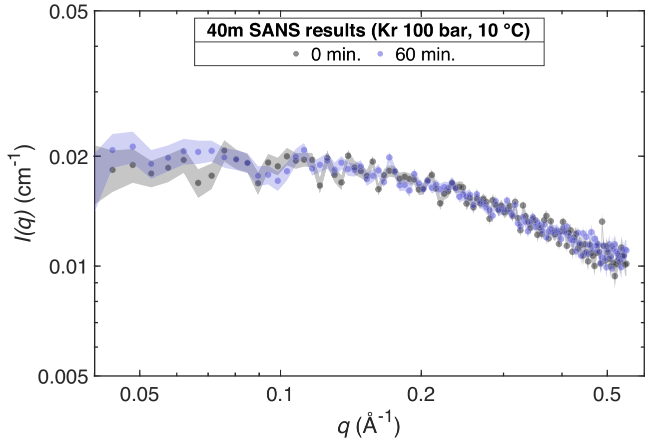

Fig. 5 | Time evolution of the neutron scattering signal at a reduced background temperature. The sample temperature is lowered to 10 °C by adjusting the stage temperature of the high-pressure chamber. Unlike the previous results obtained at 25 °C, the neutron scattering signal remains stable over time, suggesting a temperature-dependent cluster lifetime. The horizontal axis shows the scattering vector q, and the vertical axis shows the scattering intensity $I(q)$. The shaded regions represent errors reflecting both neutron counting statistics and the standard deviation resulting from circular averaging within each q-bin.

This study provides experimental evidence for non-equilibrium phase separation in SCFs. While previous research on SCF systems has primarily focused on equilibrium conditions, our findings demonstrate that rapid thermodynamic changes can induce phase separation, producing dense, liquid-like clusters. We observed opacity variations as indirect evidence of clustering, with significant increases in opacity for krypton, while helium remained transparent. To directly confirm cluster formation, we conducted SANS measurements, revealing distinct scattering signals that further support the existence of mesoscopic inhomogeneities within the SCF. An important implication of our findings is that SCFs in industrial applications often experience dynamic pressure and temperature fluctuations rather than remaining in strict equilibrium. The tendency to form dense clusters under such conditions will affect mass transport, solubility, and reactivity. Understanding these non-equilibrium effects expands our knowledge of

SCF phase behavior and underscores their importance in the design and use of SCF technologies.

Methods

High-pressure system

The high-pressure supercritical fluid generation system used in this study is identical to that described in ref. 19. The compressor, which increases the pressure via cyclic compression-expansion of pistons, is connected to the high-pressure chamber using stainless-steel hoses (Swagelok SS-FX4TA4TA4). These hoses provide flexibility to the setup, facilitating a modular configuration of the high-pressure system. To further enable modularity, quick connectors (Swagelok SS-QF4-S and SS-QF4-B) are attached at the ends of the hoses and the inlet of the chamber, allowing the high-pressure chamber to be detached and transported independently after the system is pressurized. The system includes two valves: one is used for venting and reducing the internal pressure, while the other is located at the chamber inlet and isolates the high-pressure chamber.

In this study, two types of high-pressure chambers were employed. The first is a cubic-shaped stainless-steel chamber (side length: 65 mm) with SAE J1926-1 standard 1 1/16”-12-UN threaded ports on all six faces, each featuring O-ring grooves. Five of these ports are equipped with viewports (Rayotek 101117C) for optical diagnostics, while the remaining port fills the chamber with pressurized fluid. The second high-pressure chamber is designed for SANS experiments. The stainless steel main body has a 7/16-20 UNF threaded inlet on the bottom side, through which high-pressure fluid is injected. The chamber has 1-inch diameter holes on the front and rear sides, where 1-inch aluminum windows are mounted. The distance between the two windows is 5 mm, which defines the neutron beam path length through the sample. Each window is sealed with an O-ring and secured by a cover plate that compresses the O-ring, ensuring the chamber remains leak-tight under high pressure. The chamber assembly, including the main body and cover plates, measures approximately $35 \times 51 \times 25\ mm^3$. The SANS chamber can maintain the internal pressure for a long time without any detectable leakage (Supplementary Methods, Supplementary Fig. 1).

Temperature drop experimental procedure

A thermocouple (Fluke 80PK-27) is used to measure the temperature drop from the rapidly expanding fluids. It is connected to a digitizer (Keysight DAQ970A), which records the temperature drop as the high-pressure fluid quickly expands when the valve opens. The thermocouple is placed 10 mm from the valve exit to ensure accurate temperature readings while minimizing disturbance to the fluid flow. The internal pressure of the chamber is simultaneously measured during each temperature measurement to reduce errors caused by valve opening speed.

Neutron scattering experimental procedure

The SANS experiment begins by filling the high-pressure chamber with krypton gas until the internal pressure, monitored by a pressure gauge, reaches 100 bar. Once the target pressure is reached, the compressor is turned off, the chamber valve is closed, and the chamber is detached. The high-pressure chamber, now containing supercritical krypton, is mounted on the sample stage of the neutron beamline, where time-resolved scattering measurements are performed. Because cluster decay occurs immediately after pressurization, measurements are initiated within 30 s of reaching the target pressure. Scattering signals were recorded with an exposure time of 60 s (Supplementary Methods, Supplementary Fig. 2). A background measurement was obtained using the SANS chamber filled with krypton at 1 bar and subtracted from all experimental data. Some datasets were averaged over 2-min intervals (Fig. 3b), and coarse binning of the q-range was applied (Fig. 3c) to reduce noise.

Data availability

All relevant data supporting this study are available from the authors (J.L. and G.Y.) upon reasonable request.

Received: 12 April 2025; Accepted: 5 August 2025;
Published online: 21 August 2025

References

1. Gorelli, F., Santoro, M., Scopigno, T., Krisch, M. & Ruocco, G. Liquidlike behavior of supercritical fluids. *Phys. Rev. Lett.* **97**, 245702 (2006).
2. Simeoni, G. G. et al. The widom line as the crossover between liquid-like and gas-like behaviour in supercritical fluids. *Nat. Phys.* **6**, 503–507 (2010).
3. Brazhkin, V. V., Fomin, Y. D., Lyapin, A. G., Ryzhov, V. N. & Trachenko, K. Two liquid states of matter: a dynamic line on a phase diagram. *Phys. Rev. E* **85**, 031203 (2012).
4. Brazhkin, V. V. et al. "liquid-gas” transition in the supercritical region: fundamental changes in the particle dynamics. *Phys. Rev. Lett.* **111**, 145901 (2013).
5. Banuti, D. Crossing the widom-line - supercritical pseudo-boiling. *J. Supercritic. Fluids* **98**, 12–16 (2015).
6. Prescher, C. et al. Experimental evidence of the frenkel line in supercritical neon. *Phys. Rev. B* **95**, 134114 (2017).
7. Bryk, T. et al. Behavior of supercritical fluids across the “frenkel line”. *J. Phys. Chem. Lett.* **8**, 4995–5001 (2017).
8. Pipich, V. & Schwahn, D. Densification of supercritical carbon dioxide accompanied by droplet formation when passing the widom line. *Phys. Rev. Lett.* **120**, 145701 (2018).
9. Schienbein, P. & Marx, D. Investigation concerning the uniqueness of separatrix lines separating liquidlike from gaslike regimes deep in the supercritical phase of water with a focus on widom line concepts. *Phys. Rev. E* **98**, 022104 (2018).
10. Maxim, F. et al. Visualization of supercritical water pseudo-boiling at widom line crossover. *Nat. Commun.* **10**, 4114 (2019).
11. Pipich, V. & Schwahn, D. Polymorphic phase transition in liquid and supercritical carbon dioxide. *Sci. Rep.* **10**, 11861 (2020).
12. Fomin, Y. D., Ryzhov, V. N., Tsiok, E. N., Brazhkin, V. V. & Trachenko, K. Crossover of collective modes and positive sound dispersion in supercritical state. *J. Phys. Condensed Matter* **28**, 43LT01 (2016).
13. Brazhkin, V. V., Fomin, Y. D., Lyapin, A. G., Ryzhov, V. N. & Trachenko, K. Universal crossover of liquid dynamics in supercritical region. *JETP Lett.* **95**, 164–169 (2012).
14. Brazhkin, V. V. et al. Comment on “behavior of supercritical fluids across the frenkel line”. *J. Phys. Chem. B* **122**, 6124–6128 (2018).
15. Bryk, T. et al. Reply to “comment on behavior of supercritical fluids across the frenkel line”. *J. Phys. Chem. B* **122**, 6120–6123 (2018).
16. Taylor, L. T. *Supercritical Fluid Extraction* (Wiley, 1996).
17. Rai, A., Mohanty, B. & Bhargava, R. Supercritical extraction of sunflower oil: a central composite design for extraction variables. *Food Chem.* **192**, 647–659 (2016).
18. Bellan, J. *High-Pressure Flows for Propulsion Applications* (AIAA, 2020).
19. Lee, S. et al. Quasi-equilibrium phase coexistence in single component supercritical fluids. *Nat. Commun.* **12**, 4630 (2021).
20. Lee, S., Lee, J., Yoon, Y. D., Kim, D. E. & Yun, G. Characterization of strongly coupled plasmas produced in argon supercritical fluids. *Plasma Phys. Controlled Fusion* **64**, 095010 (2022).
21. Han, Y.-S. et al. A new 40m small angle neutron scattering instrument at Hanaro, Korea. *Nuclear Instrum. Methods Phys. Res. Section A Accelerators, Spectrometers, Detectors Associated Equipment* **721**, 17–20 (2013).
22. Sears, V. F. Neutron scattering lengths and cross sections. *Neutron News* **3**, 26–37 (1992).
23. Howell, J., Siegel, R. & Mengüç, M. P. *Thermal Radiation Heat Transfer* (Academic Press, 2010).
24. Cox, A. J., DeWeerd, A. J. & Linden, J. An experiment to measure Mie and Rayleigh total scattering cross sections. *Am. J. Phys.* **70**, 620–625 (2002).

25. Sinnock, A. C. & Smith, B. L. Refractive indices of the condensed inert gases. *Phys. Rev.* **181**, 1297–1307 (1969).
26. Jeffries, C. M. et al. Small-angle x-ray and neutron scattering. *Nat. Rev. Methods Primers* **1**, 70 (2021).
27. Sato, T. et al. Structural difference between liquidlike and gaslike phases in supercritical fluid. *Phys. Rev. E* **78**, 051503 (2008).
28. Caponetti, E., Floriano, M. A., Di Dio, E. & Triolo, R. On the shape of the radial distribution function of an assembly of monodisperse ellipsoidal scatterers. *J. Appl. Crystallogr.* **26**, 612–615 (1993).
29. Linstrom, P. & Mallard, W. NIST chemistry webbook, NIST standard reference database number 69. *NIST Chemistry WebBook, NIST Standard Reference Database Number 69* (National Institute of Standards and Technology, 2025).

Acknowledgements

This work was supported by the National Research Foundation of Korea (NRF) (grant No. RS-2024-00349684) and the Korea Atomic Energy Research Institute (internal grant No. 2710007349) funded by the Ministry of Science and ICT of Korea. This work was also supported by the Glocal University 30 project funded by the Ministry of Education. A portion of this research used resources at the Spallation Neutron Source, a DOE Office of Science User Facility operated by the Oak Ridge National Laboratory. The beam time was allocated to EQ-SANS on proposal number IPTS-33852.

Author contributions

G.Y. proposed the original idea and conceived the project. J.L. designed the high-pressure chamber system. J.L., Y.K., and J.D.J. performed the experiments. J.L. carried out the data processing. J.L., C.D., and M.Y.H. carried out the data analysis. J.L. and G.Y. wrote the manuscript. G.Y. supervised the project. All authors contributed to discussions of the results and reviewed the manuscript.

Competing interests

The authors declare no competing interests.

Additional information

Supplementary information The online version contains supplementary material available at https://doi.org/10.1038/s42005-025-02263-2.

Correspondence and requests for materials should be addressed to Gunsu Yun.

Peer review information *Communications Physics* thanks Sergey Khrapak and the other, anonymous, reviewer(s) for their contribution to the peer review of this work. A peer review file is available.